J. Fluid Mech., (2013), *vol.* 724, *pp.* 704–733. © Cambridge University Press 2013. This is a work of the U.S. Government and is not subject to copyright protection in the United States.

doi:10.1017/jfm.2013.185

Flow physics in the turbulent near wake of a flat plate

Man Mohan Rai†

NASA Ames Research Center, Moffett Field, CA 94035, USA

(Received 13 September 2012; revised 2 April 2013; accepted 9 April 2013; first published online 8 May 2013)

The symmetric near wake of a flat plate with a circular trailing edge, exhibiting pronounced shedding of wake vortices, is investigated via a direct numerical simulation. The separating plate boundary layers are turbulent and statistically identical. The present study focuses on the vortical structures, the distribution of phase-averaged velocity statistics and vorticity fluctuations in the near wake. Braid and vortex core regions are investigated via contours of instantaneous vorticity and pressure with an emphasis on the three-dimensionality of near-wake structures. Rib vortices are observed in the braids. The vortex cores are populated with both ribs that wrap themselves around the cores and spanwise-elongated regions of spanwise vorticity near the centres of the cores. Production terms in the transport equations for phase-averaged fluctuating vorticity show that stretching of rib vortices via the phase-averaged strain rate produces significantly less turbulent vorticity than turbulent stretching in the braids and cores.

Key words: turbulence simulation, vortex shedding, wakes

1. Introduction

The near and intermediate wakes of aerofoil sections used in turbines and compressors are of considerable engineering importance. The near wake is of interest in trailing edge design and the intermediate wake is of interest in understanding and predicting flow transition and unsteady loads on downstream aerofoils. The magnitude of the periodic fluctuation, due to vortex shedding, and its contribution to the total fluctuations in the velocity and pressure is necessary to accurately compute unsteady aerofoil loads. Thus, insight into wake flows is essential to the design process. Turbulence models and design criteria are just a couple of areas that would benefit from a better comprehension of wakes.

The majority of the published data for turbulent wakes that are preceded by turbulent boundary layers deals with thin plates. Chevray & Kovasznay (1969) provide one of the earliest of such measurements in the turbulent wake of a thin flat plate. The ratio of the boundary layer momentum thickness to the trailing edge thickness of the plate (θ/D) is 23.2. The thickness of the trailing edge in wall coordinates (based on the wall shear velocity at the end of the plate) is 3.0 and hence smaller than the

† Email address for correspondence: man.m.rai@nasa.gov

https://doi.org/10.1017/jfm.2013.185 Published online by Cambridge University Press

viscous sublayer. The boundary layers merge smoothly to form the wake and vortex shedding is absent.

However, in many instances such as turbine aerofoils, unlike the experiment discussed above, the ratio of the momentum thickness of the boundary layer (at the trailing edge) to the trailing edge thickness is not large. For reasons of manufacturability, cost and reliability, the trailing edge thickness may be comparable to or greater than the boundary layer momentum thickness. Ratios close to or smaller than 1.0 are of interest from an engineering point of view. Here the boundary layers do not merge smoothly to form the wake. Instead we have large-scale vortex formation. Turbulent structures are embedded in the shed vortices. Thus, these wakes share some attributes with low- to moderate-Reynolds-number cylinder wakes that have been studied extensively ($1200 \leqslant Re_D \leqslant 150\,000$, Re_D based on cylinder diameter).

Experimental techniques have generated a large percentage of the cylinder wake data that have provided us with the current state of understanding of the subject. More recently computational techniques such as large eddy simulations (LES) and direct numerical simulations (DNS) have been used to compute cylinder wakes, and the data from these simulations have refined our understanding of such flows and provided new insights. These cylinder-wake investigations focus on a Reynolds number range where the cylinder boundary layer is laminar (subcritical range). However, from an engineering point of view, there is considerable interest in the situation where the upper and/or lower boundary layer of an aerofoil is turbulent, and these turbulent boundary layers separate from the aerofoil to contribute to the formation of the wake downstream. In the case of cylinders of small diameter, boundary layer transition only occurs at relatively large unit Reynolds numbers. However, in the case of aerofoils, the boundary layer has the opportunity to transition to turbulence on the aerofoil surface at a substantially lower unit Reynolds number (the characteristic length of the aerofoil is typically one to two orders of magnitude larger than the trailing edge diameter). This transition occurs unless there is a favourable pressure gradient that results in the boundary layer remaining laminar or transitional. In addition, in the aerofoil case Re_θ (θ is the boundary layer momentum thickness just upstream of the trailing edge) and Re_D are independent parameters.

Here we investigate the wake of a flat plate with turbulent boundary layers that exhibits pronounced vortex shedding. Unlike the cylinder, and more in keeping with the aerofoil, the boundary layers are turbulent even though Re_D is modest (10 000). With the flat plate there is also the advantage of not having the complexities of the aerofoil (such as pressure gradients and specificity of the geometry) in a first investigation. It is also a case that can be duplicated/extended by other researchers in a straightforward manner. Among the computational approaches available to investigate such flows, DNS is particularly suitable because it does not require any modelling of turbulence and transition. The Reynolds numbers encountered in many turbines and compressors are moderate (and so also in the current investigation) and thus a short-span DNS can be obtained on current supercomputers.

A first computation of the wake of a thick flat plate with a circular trailing edge (CTE) is provided by Rai (2010*a*). The objectives of this investigation were to initiate the computational study (via DNS) of turbulent wakes preceded by turbulent boundary layers in the context of thick, blunt trailing edges, investigate some of the near wake flow physics, and compare the computed results with experimental data. A high-order accurate, upwind-biased finite-difference method for curvilinear grids, described in Rai (2010*b*) was utilized for this purpose. Both the upper and lower boundary layers on the plate undergo transition to turbulence before encountering the trailing edge.

https://doi.org/10.1017/jfm.2013.185 Published online by Cambridge University Press

X/D	10.0	20.0	40.0
Matsumura and Antonia	85.3 %	70.7 %	49.0 %
Rai (2008)	80.6 %	65.0 %	47.8 %

TABLE 1. Comparison of computed and experimental ratio of energies in the periodic and total signals.

Two cases are computed. The first is at $Re_D = 3900$. The results from this case are compared with computed results for subcritical flow about a cylinder that was obtained in Rai (2008) at the same Reynolds number. The second case attempts to mimic the experiment of Haji-Haidari & Smith (1984). The Reynolds number based on the boundary layer thickness at the end of the plate and Re_D (=32 000) are close to those of Haji-Haidari & Smith (1984). The computed mean velocity profile on the plate, near the trailing edge, agrees well with the log-law and fairly well with the experimental data. The computed streamwise Reynolds stress profile at this location also agrees well with the experimental data thus establishing the similarity of the computed and experimental boundary layers before they detach from the plate surface. The computed velocity and Reynolds stress profiles in the wake agree with experimental data in the very near wake but differ somewhat downstream.

Additional comparisons of computed wake data (via DNS) with experimental data for the case of cylinders at two Reynolds numbers are provided in Rai (2008). Computed cross-stream profiles of fluctuating stresses and centreline velocity spectra for one of the cases are compared with experimental data and found to be in agreement. The magnitude of the periodic fluctuation and its contribution to the total fluctuations in the velocity and pressure are important in determining the unsteady loads to be used in designing turbomachinery. The computed ratio of the energies in the periodic and total signals (cross-stream component of velocity) for the case of the cylinder at $Re_D = 5830$, along the centreline, are compared with experimental data from Matsumura & Antonia (1993) in table 1. The comparison shows the ability of the numerical method used to compute this ratio accurately. The computational method used in the present investigation and in Rai (2008, 2010*a*) are the same. The energy contained in the periodic component of cross-stream velocity in Rai (2010*a*) at the locations $x/D = 2.5$, 4.5 and 6.5 are 0.197, 0.148 and 0.120, respectively. A 40 % reduction is obtained between $x/D = 2.5$ and 6.5; a fact of interest in computing the unsteady loads mentioned earlier.

The investigations reported in Cantwell & Coles (1983), Kiya & Matsumura (1988) and Hayakawa & Hussain (1989) are of importance to the present study. They are referred to hereafter as the investigations of CC (1983), KM (1988) and HH (1989), respectively. In CC (1983) the turbulent near wake of a circular cylinder ($Re_D = 140\,000$) is investigated with the aid of time- and phase-averaged velocity statistics. The authors make several inferences regarding the regions and mechanisms of turbulence production, the scales at which turbulence is produced, the importance of the pressure-strain term in redistributing turbulent kinetic energy (TKE) and the role of saddle points in entrainment and turbulence production. KM (1988) analysed experimentally obtained wake data for a normal plate (face normal to the flow direction) to determine the fluctuating energy (random component) in the three velocity

https://doi.org/10.1017/jfm.2013.185 Published online by Cambridge University Press

components at different phases and within specified frequency ranges. A surprising finding of KM (1988) is that the real part of the cross-spectrum of the randomly fluctuating streamwise and cross-stream velocity signals (turbulent shear stress) shows a dominant peak at about half the shedding frequency (ω_{st}) whereas the power spectra of the three velocity signals show peaks between ω_{st} and $2\omega_{st}$. A possible explanation for this phenomenon based on spanwise rib vortex placements in the braid is provided in KM (1988). The three-dimensionality of organized structures in the intermediate wake of a cylinder is investigated in HH (1989). Measurements of spanwise and transverse vorticity at $x/D = 20$ and 40 are provided. Two-point correlations in the spanwise direction and spanwise vorticity are used to explore both the three-dimensionality of shed vortices and the increasing lack of coherency with increasing streamwise distance. The findings reported by CC (1983), KM (1988) and HH (1989), as pertinent to the current investigation, are discussed later in the text.

1.1. *Current objectives*

In the present investigation, data from a recent DNS of a flat plate wake using the methodology of Rai (2010*a*) are analysed. The DNS has been performed on a grid that provides adequate resolution until $x/D = 13.75$ instead of $x/D = 10.0$ as in Rai (2010*a*). The present computation extends over a time period that is considerably longer than in Rai (2010*a*) (a factor of 12.5). The Reynolds numbers based on plate length and thickness (diameter of CTE) are 1.255×10^6 and 10 000, respectively and are different than in Rai (2010*a*). The separating boundary layers are turbulent and statistically identical. Thus the wake is statistically symmetric. The transitional/turbulent boundary layers are also computed via DNS.

Fluctuations in velocity in the wake arise from both random turbulence and quasi-periodic fluctuations caused by vortex shedding. Distributions of the phase-averaged periodic and random components of streamwise and cross-stream normal intensities and fluctuating shear stress are provided in CC (1983). The main purpose of the present investigation is to study the flow physics encountered in the near wake of the flat plate. As a part of this effort the computed distributions of the phase-averaged intensities and shear stress (random component) are compared with those of CC (1983) and the commonalities and differences between the two are identified. Here we explain critical features of the distribution of the turbulent stresses with the aid of both the turbulence production term in the corresponding transport equations (budget) and features of the phase-averaged velocity distributions. These velocity distributions themselves are understood as induced by the nearby shed vortices. Where possible, simple physical explanations of the observed features in the stresses are also provided. In addition, the phase-averaged distribution of the squares of the components of fluctuating vorticity, and the production terms due to the fluctuating and phase-averaged strain rates in the corresponding transport equations are provided. One objective is to compare the magnitudes of the three fluctuating components; another is to compare the relative importance of the two production terms in the braids and vortex cores.

The visualization of the vortical structures of the near wake, such as shed vortices and rib vortices, via instantaneous vorticity and pressure distributions is an important aspect of this investigation. As in HH (1989) we study the three-dimensionality of the braids and shed vortices. Another objective here is to determine if the cross-spectrum as in KM (1988) exhibits a peak at about half the shedding frequency, and if it does, to determine whether indeed the phenomenon can be attributed to rib placements in the braid.

https://doi.org/10.1017/jfm.2013.185 Published online by Cambridge University Press

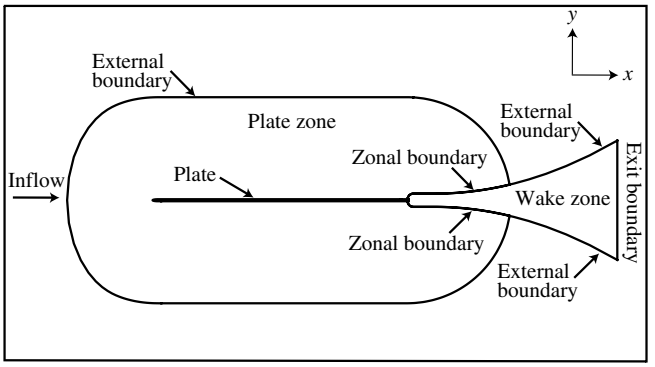


FIGURE 1. Midspan plate section and multiple zone discretization of the computational region (coordinate system origin actually located at the centre of the CTE).

2. Computational grid and numerical method

The computational region is divided into two zones to facilitate grid generation and provide adequate grid resolution for the wake. Figure 1 shows the plate cross-section and the two zones that comprise the computational region. The three-dimensional zones and grids are obtained by uniformly spacing copies of these two-dimensional zones in the spanwise direction (z). The plate zone is bounded by four boundaries: the plate surface (excluding the trailing edge), an external boundary and two zonal boundaries (top and bottom) that interface with the wake zone. It captures the inviscid flow field upstream of the trailing edge and the plate boundary layers. The leading edge of the plate is an ellipse. The wake zone provides adequate resolution for the detached shear layers, the recirculation region and the wake. The boundaries of this zone include the CTE, upper and lower boundaries and the exit boundary. The upper and lower boundaries consist of a zonal boundary segment that interfaces with the plate zone, and a segment that serves as an external boundary.

The external boundary of the plate zone is placed $50.0D$ from the plate surface, where D is the diameter of the CTE (D is also the thickness of the plate). The length of the plate is $125.5D$. The exit boundary of the wake zone is $104.0D$ from the centre of the CTE and its vertical extent is $81.0D$. The vertical extent of the wake zone in the vicinity of the trailing edge, where its upper and lower boundaries are horizontal, is $9.0D$ and is large enough to completely contain the wake. The spanwise extent of the computational region is $4.0D$. The streamwise extent of the well-resolved region of the wake zone extends to $13.75D$ from the CTE (origin of the coordinate system).

Figure 2 shows representative grids in the vicinity of the trailing edge in both zones. The grid in the wake zone transitions from curvilinear near the trailing edge to rectangular downstream. Beyond $13.75D$, the wake grid coarsens gradually in the x direction. In addition to reducing the computational costs incurred, this coarsening dissipates the wake to a degree that inviscid exit boundary conditions can be employed at the exit boundary of the wake zone.

The wake grid was constructed with 541 grid points in the x direction, 311 in the y direction and 256 in the z direction (about 43×10^6 grid points). The resolution achieved in these directions at $x/D = 10.0$, $y/D = 0.0$, is approximately $\Delta x/\eta = 4.0$, $\Delta y/\eta = 4.0$ and $\Delta z/\eta = 2.1$. Here η is the computed Kolmogorov length scale at this location. Both the grids have the same spacing in the wall-normal direction at the plate

https://doi.org/10.1017/jfm.2013.185 Published online by Cambridge University Press

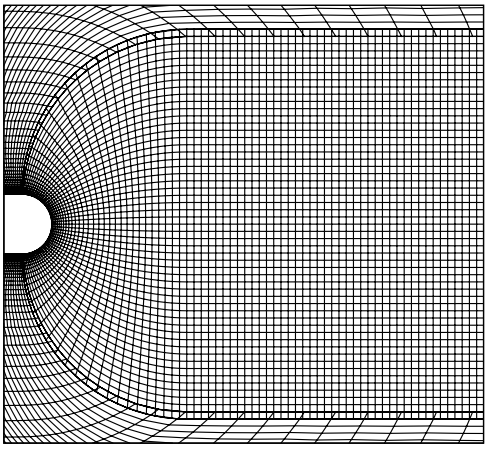


FIGURE 2. Representative grids in the plate and wake zones, in the vicinity of the CTE.

surface, $\Delta n = 0.002D$. The grid resolution in the plate grid in the x, y and z directions is $\sim$18.0, 0.84 and 6.5 wall units, respectively, based on the wall shear velocity near the end of the plate. The adequacy of the grid resolution and boundary placement is discussed further in appendix A.

The high-order accurate upwind-biased method of Rai (2010*a*) (see appendix A for a few details) is used to compute the flow over the plate as well as in the wake. The boundaries that contain the plate and wake grids can be broadly classified as natural and zonal boundaries. The natural boundaries include the external boundary of the plate grid, the surface of the plate, the exit boundary of the wake grid, the segments of the upper and lower boundaries of the wake grid labelled as 'external boundary' in figure 1, and the boundaries in the z direction. The upstream segment of the upper boundary between the plate and wake grids is an example of the zonal boundaries used in the computation. Both the natural and zonal boundary conditions used in this study are discussed in Rai (2010*a*). No-slip/adiabatic wall conditions are used on the plate surface and the trailing edge circle. Wall blowing/suction, as described in Rai (2010*a*), is implemented on a short segment on both the upper and lower surfaces of the plate to induce transition to turbulence.

3. Results

The plate/wake DNS was performed at a Mach number of 0.2. The Reynolds numbers based on the trailing edge diameter and plate length are 10 000 and 1 255 000, respectively. Initial transients were eliminated by integrating the governing equations over a time interval corresponding to a large number of trailing edge vortex-shedding periods. Turbulence statistics were obtained over $\sim$100 shedding periods (175 760 time steps with 1750 time steps per period). They were averaged in the spanwise direction and in time or at constant phase as appropriate. The computed Strouhal number was 0.173.

3.1. *The plate section*

Although the principal objective here is the investigation of the turbulent wake of the flat plate it is necessary to establish that the plate boundary layer is indeed turbulent

https://doi.org/10.1017/jfm.2013.185 Published online by Cambridge University Press

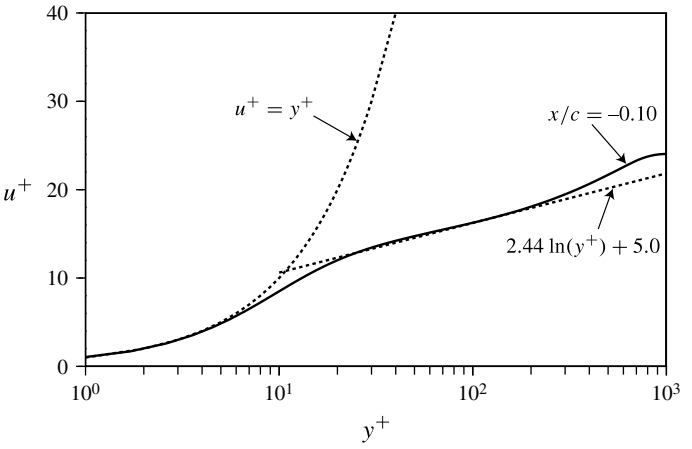


FIGURE 3. Mean velocity profile at 90 % of plate length.

before it detaches from the plate surface. Figure 3 shows the mean velocity profile in the turbulent region at 90 % of the length of the plate (12.55D upstream of CTE). The dashed lines represent the near-wall behaviour and the log-law; u^+ is the streamwise component of velocity normalized by the wall shear velocity and y^+ is the wall-normal distance in wall coordinates. The agreement with the linear profile and the log-law is good. The profile shows a distinct 'wake' region that diminishes downstream because of a favourable pressure gradient near the trailing edge. Velocity statistics obtained on the upper and lower plate surfaces are nearly identical. Figure 3 shows an average of data obtained on these two surfaces.

The computed turbulent normal intensity and shear stress profiles are compared with the experimental data of Karlson & Johansson (1988) in Rai (2011) and, are found in good agreement. For example, the average percentage error in root mean square (r.m.s.) turbulence intensity (u and v components only, at Re_θ of $\sim$2400) is 6.7 %. The average percentage error in w_{rms} at Re_θ of $\sim$1750 is 4.3 %. Here and in the rest of the article u, v and w are the velocities in the x, y and z directions, respectively, and p is the pressure. The shape factor variation on the plate surface showed a rapid reduction through transition followed by a nearly constant region thereafter except near the trailing edge; it is approximately 1.40 at 90 % of the plate length. Thus, the flow at this location closely approximates a turbulent boundary layer.

3.2. *Wake flow*

The computed phase-averaged normal intensities and shear stress in the near wake are now compared with those of CC (1983) to identify commonalities and differences. A visualization of the vortical structures of the near wake via instantaneous vorticity and pressure distributions is also provided in this section. As in HH (1989) and KM (1988) the three-dimensionality of shed vortices and the dominant contributing frequency to the random component of shear stress are investigated. Figure 4, showing contours of instantaneous spanwise velocity in a (x, y) plane, is provided as an introduction to the flat plate wake. Here and in other figures showing instantaneous flow features, the chosen time instant corresponds to 54 080 time steps (n) after the initiation of time sampling ($\sim$30.9 shedding periods). The shed vortices and the embedding of the turbulent vortices within the shed vortices are evident. The signature of the rib

https://doi.org/10.1017/jfm.2013.185 Published online by Cambridge University Press

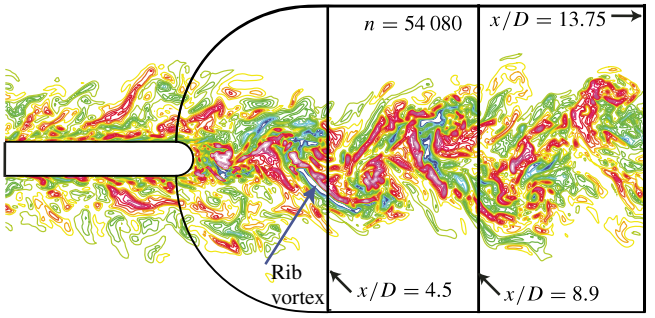


FIGURE 4. Contours of instantaneous spanwise velocity in a (x, y) plane; red/magenta represent high/highest positive values, green/blue low/lowest negative values, yellow ≈ 0.0.

vortices in the regions between the shed vortices (long thin structures, one of them shown with a blue arrow) can be discerned. The two turbulent boundary layers and the clear demarcation between the wake and the outer flow are also evident. The wake is contained well within the wake zone in the y direction.

The fluctuating density, pressure and velocity components in the flow field are assumed to contain a mean component, a periodic component at shedding frequency ω_{st} (and harmonics thereof) and a random turbulent component as in Reynolds & Hussain (1972). Thus, a flow variable q is written as

$$q = \bar{q} + q' + q'' \tag{3.1}$$

where $\bar{q}$ is the mean value, and q' and q'' are the random and periodic fluctuating components, respectively. The phase-averaged value $\langle q \rangle$ (average at constant phase) is given by

$$\langle q(\varphi) \rangle = \bar{q} + q''(\varphi) \tag{3.2}$$

where ϕ is the phase, $0.0 \leqslant \phi \leqslant 1.0$. The computed data were averaged in the z direction to obtain both the time averages and phase averages since the flow is homogeneous in this direction. The phase-averaging method used here is described in appendix B.

In the following contour plots the colours blue/green represent negative values (deep blue representing the lowest value) of the term/quantity being discussed. Orange, red and magenta represent positive values (magenta bordering on white representing the highest value). Shades of yellow represent values close to zero. Thus, figures pertaining to distributions of normal intensity do not contain shades of blue or green. In figures containing multiple subplots of contours, the minimum and maximum value specified and the increment between consecutive contour values is the same. Thus, contours/features in the subplots can be compared directly. Some of the contour plots with subplots provide a numerical value for a factor f (e.g. $f = 4.0$) for each subplot. This is the factor that the quantity in the subplot is multiplied by so that its minimum and maximum values are about the same as those in the other subplots. This operation ensures that the number of contours in each subplot is sufficient to depict features of interest.

Figure 5 shows contours of the phase-averaged spanwise vorticity (full line) and the phase-averaged pressure (dashed line), both at $\phi = 0.0$. This particular phase is close to that used in CC (1983) to discuss momentum transport (negative vortex core

https://doi.org/10.1017/jfm.2013.185 Published online by Cambridge University Press

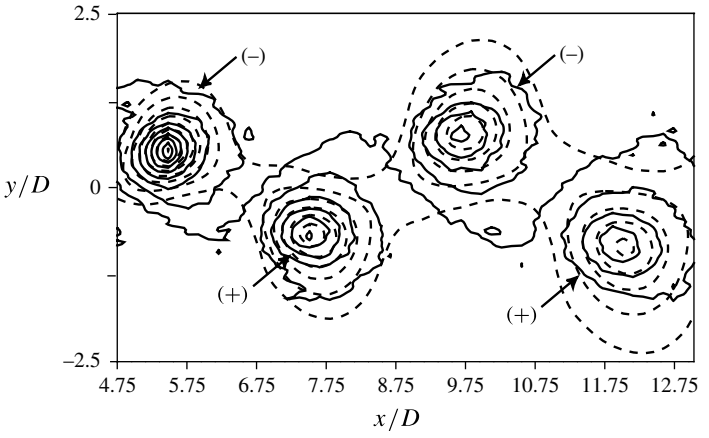


FIGURE 5. Phase-averaged spanwise vorticity and pressure contours in the wake ($\phi = 0.0$).

at $x/D = 5.5$, figure 21 in CC (1983)). The positive vortices below the centreline and negative ones above this line are evident. The pressure minima are close to the vortex cores; even the vortex shapes are captured reasonably well by the pressure contours. In the following figures pressure contours as in figure 5 are used to show the location of the cores because they are smoother than the vorticity contours (a larger sample is required to obtain smooth vorticity contours). In figure 5 consecutive cores of the same sign are about $4.2D$ apart in the region $3.0 < x/D < 8.0$ as in CC (1983).

The computed vortex spacing parameter (κ, y location of vortex core divided by x spacing of cores as defined in HH (1989)), at $x/D = 5.5$ and 10.0 are 0.13 and 0.18, respectively. The experimental value of HH (1989) at $x/D = 10.0$ is 0.20 and is close to the present value; the other experimental investigations discussed in HH (1989) report similar values. However, the estimated value at $x/D = 5.5$ in CC (1983) is 0.06 and is less than half of that obtained here. The point is made in CC (1983) that their vortices travel essentially parallel to and very close to the centreline. The magnitude of the computed peak vorticity at $x/D = 5.5$ and 10.0 are 1.60 and 0.82. The estimated experimental value of CC (1983) at $x/D = 5.5$ is $\sim$1.17 and the experimental value of HH (1989) at $x/D = 10.0$ is $\sim$1.06. Hence, the peak vorticity values obtained here are in the range obtained in CC (1983) and HH (1989). The differences in the wake flow must be kept in mind in assessing proximity to the experimental data (turbulent separating boundary layers, geometry of the wake generating body, Reynolds numbers, etc.).

3.3. *Phase-averaged normal intensity and shear stress distributions (random component)*

Contours of $\langle u'u' \rangle$ and $\langle p \rangle$ are shown in figure 6(a) ($\phi = 0.0$). The contours show the braids between successive vortices of opposite sign and maxima that are close to the vortex cores. The braids first curve upstream until they encounter the centreline and then turn downstream. They contain a second distinct maximum in $\langle u'u' \rangle$. There is a minimum in $\langle u'u' \rangle$ adjacent to each vortex core and to the corresponding braid (blue star). These last two braid related features are not seen in CC (1983) (figure 24b in CC (1983)).

The peak intensity value at $x/D = 5.5$ (negative vortex) is 0.025. The corresponding value from CC (1983) is 0.094 (estimated) and is 3.75 times as large as that obtained here. Rai (2010a) (see also references cited therein) compared wake centreline values

https://doi.org/10.1017/jfm.2013.185 Published online by Cambridge University Press

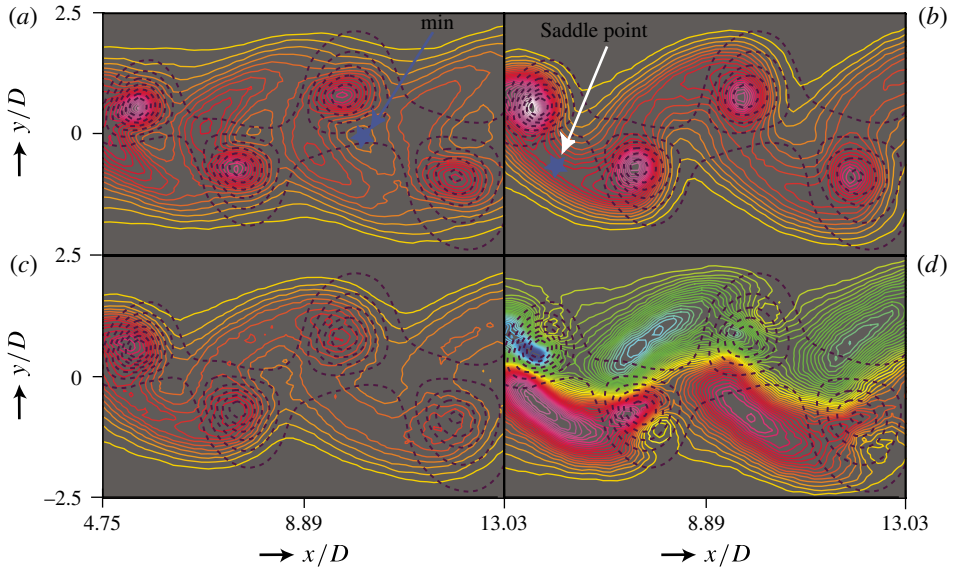


FIGURE 6. Contours of (*a*) $\langle u'u' \rangle$ ($f = 1.0$), (*b*) $\langle v'v' \rangle$ ($f = 1.0$), (*c*) $\langle w'w' \rangle$ ($f = 1.0$) and (*d*) $\langle u'v' \rangle$ ($f = 4.0$) and $\langle p \rangle$ ($\phi = 0.0$); red/magenta represent high/highest positive values, green/blue low/lowest negative values, yellow ≈ 0.0.

of mean square fluctuating velocity obtained for a cylinder (laminar boundary layers) and a flat plate with a CTE (turbulent boundary layers), both at $Re_D = 3900$. The flat plate data are consistently two to four times smaller than those obtained for the cylinder. Here, once again, presumably because of the separating boundary layers being turbulent, and separating later than in the experiment (mean separation angle is $+24.5°$ from the vertical here and is $-17.0°$ in CC (1983)) and because of differences in the ratio (θ/D) we have significant differences in intensity levels. Therefore, comparisons with the findings of CC (1983) will be qualitative and not quantitative henceforth.

Contours of $\langle v'v' \rangle$ and $\langle p \rangle$ are presented in figure 6(*b*). As in the case of $\langle u'u' \rangle$ the peaks occur close to the vortex cores. Peak intensity values decrease monotonically with increasing x. These features are observed in the data of CC (1983) as well (figure 25*b* in CC (1983)). Another feature of interest is that unlike in figure 6(*a*), the braids here contain a saddle point and not a maximum; the minimum occurs along the axis of a braid and the maximum in a direction nearly orthogonal to this axis. One of them is marked with a blue star in figure 6(*b*). The data of CC (1983) also indicate a saddle point in the braids. Figure 6(*c*) shows contours of $\langle w'w' \rangle$. They are similar to those obtained for $\langle v'v' \rangle$ (saddle point in the braid and a maximum near the vortex core). Figure 6(*d*) shows contours of $\langle u'v' \rangle$ and $\langle p \rangle$. The level of detail obtained in the computation is noticeably greater than in the experimental data of CC (1983) (figure 26*b* in CC (1983)). Regions of high $\langle u'v' \rangle$ are confined to the braids and vortex cores. As expected, the regions above the centreline show negative $\langle u'v' \rangle$ and those below the centreline show positive $\langle u'v' \rangle$. As in CC (1983), we have peaks near the cores and the braids above the centreline contain a minimum while those below contain a maximum.

To better understand the observed distribution of the phase-averaged normal intensities and shear stress we turn to the production term in the transport equations

https://doi.org/10.1017/jfm.2013.185 Published online by Cambridge University Press

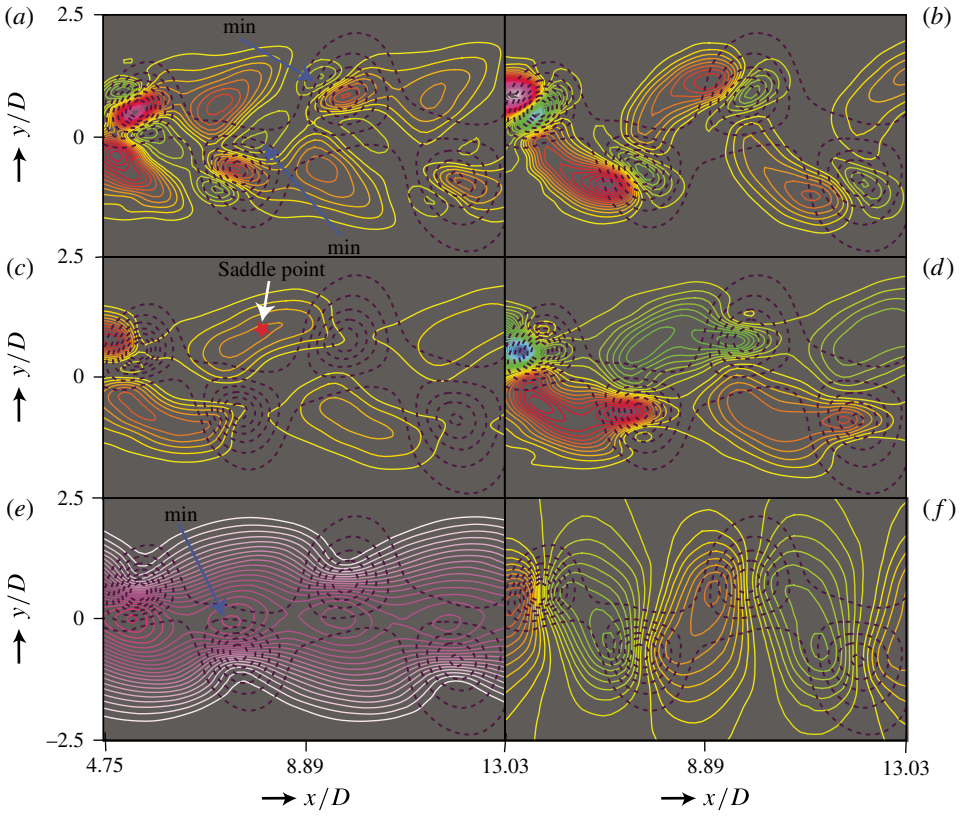


FIGURE 7. Phase-averaged production terms (*a*) P_{11} ($f = 1.0$), (*b*) P_{22} ($f = 1.0$), (*c*) 0.5 ($P_{11} + P_{22}$) ($f = 1.0$) and (*d*) P_{12} ($f = 1.0$); phase-averaged velocities (*e*) $\langle u \rangle$ and (*f*) $\langle v \rangle (\phi = 0.0)$; red/magenta represent high/highest positive values, green/blue low/lowest negative values, yellow ≈ 0.0 (in *a–d, f*).

for these stresses. For the incompressible form of the transport equations we obtain (Rai 2012)

$$P_{ij} = -\rho \left[\langle u_j' u_k' \rangle \frac{\partial \langle u_i \rangle}{\partial x_k} + \langle u_i' u_k' \rangle \frac{\partial \langle u_j \rangle}{\partial x_k} \right] \tag{3.3a}$$

where ρ is the density, and u_i ($i = 1, 2, 3$) are the velocity components in the x, y and z directions (x_i). Assuming the periodic fluctuating component is absent and replacing phase averages with time averages in (3.3*a*) results in the production term reported in Mansour, Kim & Moin (1988). Figure 7(*a*) shows contours of the turbulence production term $\langle P_{11} \rangle$ in the budget of $\langle u'u' \rangle$, given by

$$P_{11} = -2\rho \left[\langle u'u' \rangle \frac{\partial \langle u \rangle}{\partial x} + \langle u'v' \rangle \frac{\partial \langle u \rangle}{\partial y} \right]. \tag{3.3b}$$

The term $\langle u'w' \rangle \partial \langle u \rangle / \partial z$ does not appear in (3.3*b*) (homogeneity in the z direction). The braid region (see figure 6*a* for the shape and location of the braid) shows significant turbulence production and contains a local maximum in production. These two features are consistent with those seen in figure 6(*a*) (high intensity in the braid

https://doi.org/10.1017/jfm.2013.185 Published online by Cambridge University Press

with a local maximum). The braids emanating from the cores first move upstream and then downstream. In the region where they turn the braids and the rib vortices contained within them are essentially vertical thus resulting in large values of u' and a maximum in $\langle u'u' \rangle$.

The vortex core shows a positive production rate that is consistent with the maximum in intensity that exists in the core. Figure 7(*e*) shows contours of $\langle u \rangle$. In the vicinity of the vortex cores the contour lines are essentially horizontal and densely packed in the vertical direction, thus indicating small values of the x-derivative and large values of the y-derivative of $\langle u \rangle$. The second term in the equation for P_{11}, containing the shear stress, is thus dominant. Since for the vortices above the centreline the velocity derivative is positive (figure 7*e*) and $\langle u'v' \rangle$ is negative (figure 6*d*), P_{11} in these vortex cores is positive. In fact, a maximum occurs near each vortex core. Physically, the presence of spanwise elongated segments of spanwise vorticity (discussed later, figure 11) and segments of rib vortices contained within the core and aligned with it both result in high values of $\langle u'u' \rangle$ and a local maximum in the core.

Figure 7(*a*) also shows a band adjacent to each braid extending from one vortex core to the next where there exists turbulence consumption (negative value of production). One such band is identified with two arrows; it contains two local minima. This band is consistent with the behaviour in figure 6(*a*) where we see a band of low intensity adjacent to each braid (although only one local minimum can be identified within the low-intensity band). The region occupied by one of the minima (upward arrow) is not a part of the braid with its rib vortices (figure 9). As mentioned earlier, the braids in the regions where they emanate from the cores, move upstream before turning downstream near the centreline thus avoiding this region.

Figure 7(*b*) shows contours of the production term P_{22} in the budget of $\langle v'v' \rangle$, given by

$$P_{22} = -2\rho \left[\langle u'v' \rangle \frac{\partial \langle v \rangle}{\partial x} + \langle v'v' \rangle \frac{\partial \langle v \rangle}{\partial y} \right]. \tag{3.3c}$$

The entire braid region here shows positive values for the production term; this is consistent with the high levels of intensity in this region seen in figure 6(*b*). There is a peak in production upstream of each core. The rib vortices and the braids in these regions are essentially aligned with the x direction resulting in large values of v' and $\langle v'v' \rangle$, and a maximum in P_{22}. However, at the vortex cores we have consumption instead of production. This can be explained by examining the distribution of $\langle v \rangle$ shown in figure 7(*f*). At the vortex cores the x-derivative of $\langle v \rangle$ is large and the y-derivative is small. Thus, the first term in (3.3*c*) is dominant. The turbulent shear stress is negative at all of the vortex cores above the centreline and so is the x derivative of the $\langle v \rangle$. This results in negative values of P_{22} in the upper cores. For similar reasons, this term is negative at all of the cores below the centreline. The turbulent transport term for $\langle v'v' \rangle$ is nearly zero at the centres of the cores (Rai 2012). Thus, it is most probably the velocity pressure gradient term that sustains the peak in intensity at the centre. The physical reasons for the peak in $\langle v'v' \rangle$ near the core are the same as those for a peak in $\langle u'u' \rangle$.

Figure 7(*c*) shows the distribution of the production term in the phase-averaged TKE, (3.3*a*), and also from CC (1983)

$$P_{TKE} = -\left[\langle u'u' \rangle \frac{\partial \langle u \rangle}{\partial x} + \langle u'v' \rangle \left(\frac{\partial \langle v \rangle}{\partial x} + \frac{\partial \langle u \rangle}{\partial y} \right) + \langle v'v' \rangle \frac{\partial \langle v \rangle}{\partial y} \right]. \tag{3.3d}$$

https://doi.org/10.1017/jfm.2013.185 Published online by Cambridge University Press

Regions of negative production are negligible in this combined production term, demonstrating that the positive production rate of $\langle u'u' \rangle$ more than compensates for the negative rate obtained for $\langle v'v' \rangle$ in the vortex cores. Similarly the negative production rate of $\langle u'u' \rangle$ adjacent to the braid region is compensated for by the positive production rate of $\langle v'v' \rangle$. The production rate for $\langle w'w' \rangle$ is zero because $\langle w \rangle$ is zero everywhere. Here, again, it is probably the velocity pressure gradient term that contributes to the sustenance of $\langle w'w' \rangle$. Clearly the stretching of rib vortices (amplification of streamwise and transverse vorticity) in the braid contributes significantly to the creation of w'.

Figure 7(*d*) shows contours of the production term in the transport equation for $\langle u'v' \rangle$ given by

$$P_{12} = -\rho \left[\langle u'u' \rangle \frac{\partial \langle v \rangle}{\partial x} + \langle v'v' \rangle \frac{\partial \langle u \rangle}{\partial y} \right]. \tag{3.3e}$$

This term is for the most part negative above the wake centreline and positive below the centreline. Hence, we have production of shear stress both above and below the centreline. The lobes above and below have two extrema each, one near the vortex core and the second in the braid region. This is consistent with the distribution of shear stress in figure 6(*d*). To better understand the distribution of P_{12} in the braids consider an upwardly slanted braid region connecting a positive vortex to a negative one. Note from figure 7(*e*) and (*f*) that both the x-derivative of $\langle v \rangle$ and the y-derivative of $\langle u \rangle$ are positive in this region. The second feature is true above the minimum in $\langle u \rangle$ located close to the centreline (one of the minima is shown with an arrow). Since the intensities are also positive, we have production of $\langle u'v' \rangle$ in the braid (P_{12} is negative). The peak in shear stress near the cores can be explained using similar reasoning. From a physical perspective, upwardly slanted rib vortices (and pairs of them) induce a local velocity field that results in negative $\langle u'v' \rangle$.

The role of vortex stretching in turbulence production in the braid region resulting from the strain field therein (and the associated saddle point contained in the braid with the line of separation roughly aligned with the braid axis) is discussed at length in CC (1983). The computed maximum in production occurs in the braid near the peak in $\langle u'v' \rangle$ (consistent with the findings of CC (1983)). In CC (1983) the term associated with the turbulent shear stress in (3.3*d*) is the dominant contributor to the production term. However, the authors, based on an appropriate coordinate transformation (principal axes of the rate of strain tensor), show that it is not the peak in $\langle u'v' \rangle$ which results in turbulence production within the braid but the strong strain field near the saddle. The required coordinate rotation angle α, given in CC (1983), is

$$\tan(2\alpha) = \left(\frac{\partial \langle u \rangle}{\partial y} + \frac{\partial \langle v \rangle}{\partial x} \right) \Big/ \left(\frac{\partial \langle u \rangle}{\partial x} - \frac{\partial \langle v \rangle}{\partial y} \right). \tag{3.3f}$$

A similar analysis with the present data leads to the same conclusion. The approximate location of the saddle point used is shown with a red star in figure 7(*c*). The average of the velocities at the two neighbouring vortex cores was subtracted from the velocity field to locate this saddle point. The angle α was computed to be $\sim 44^\circ$ and it is nearly the same as in CC (1983) (42.7°). A feature of interest both here and in CC (1983) is that P_{TKE} is not zero near the vortex cores.

The statistical sample used to compute the phase-averaged intensities, etc., consists of approximately 100 shedding cycles. Spanwise averaging was used to increase the sample size. However, some of the production terms continue to exhibit small-amplitude high-frequency oscillations in the contours. A larger statistical sample would

https://doi.org/10.1017/jfm.2013.185 Published online by Cambridge University Press

eliminate the jitter (a probable cause is the computation of the derivatives in the production terms). A filtering technique consisting of three-point smoothing in the x direction and a low-pass filter in the y direction were applied to the production terms (Rai 2012).

Figure 6 shows that some of the observed qualitative trends in the phase-averaged data are quite similar to those obtained experimentally in CC (1983). However, quantitatively there exist substantial differences between the two studies. As discussed earlier there are significant differences between the near wakes of the cylinder and the flat plate (even comparing computations at the same Re_D and with the same trailing edge geometry). This is expected since, among the other factors mentioned earlier, Re_θ and Re_D are independent parameters for the flat plate. In fact periodic shedding may be absent when Re_θ is large compared with Re_D. A comparison of the wake flow obtained for different values of the ratio of these two Reynolds numbers would be valuable but is beyond the scope of the current investigation. A comparison of the distribution of the time-averaged and phase-averaged (periodic component) normal intensities and shear stress obtained in the present computation and in CC (1983) are provided in Rai (2011). The two sets of data are for the most part qualitatively similar.

3.4. *Vortical structures in the near wake*

The three-dimensionality of organized structures in the intermediate wake of a cylinder ($Re_D = 13\,000$) is investigated in HH (1989). Measurements of spanwise and cross-stream vorticity at $x/D = 20.0$ and 40.0 are provided. Some of the principal observations of this study that are pertinent to the present one are as follows. (i) Two-point correlations in the z direction of smoothed spanwise vorticity near the vortex cores and at y locations closer to the centreline decrease exponentially with increasing separation in the z direction. (ii) Peak vorticity levels also decrease considerably with increasing spanwise distance between the reference (x, y) plane (plane at which vortex core detection is performed) and the plane in question. These two findings indicate considerable distortion in the shed vortices. The distortion could take many forms including bending and outright rupture of the shed vortex. (iii) The data indicate the presence of rib vortices in the braid regions between successive shed vortices of opposite sign. (iv) The strength and size of these rib vortices may be similar to that of the shed vortices. (v) Any perturbation in vorticity in the braid region would tend to become aligned and organized in the direction of the principal strain (vortex stretching) and thus result in the generation of these ribs. (vi) The ribs are subject to continual stretching along the axis of the braid. (vii) The ribs, in turn, distort the shed vortices. These observations are now addressed in the context of the wake of the flat plate with turbulent separating boundary layers.

Figure 8(a) and (b) show perspective views of the wake region (up to $x/D = 7.0$) at the same instant in time as figure 4. Figure 8(a) shows the full spanwise extent of the computational region. To better depict the structures in the vortex cores, figure 8(b) shows 25 % of the spanwise extent. Two surfaces of constant streamwise vorticity (equal in magnitude), positive (red) and negative (green) are shown in figure 8(a).

Rib vortices are observed in the braid regions (arrow marks one of them); many of them are paired (positive and negative) and some are solitary. The core regions show vortical structures that evolve from the ribs. These 'evolved' vortices in the core are much more distinct in figure 8(b) which shows a surface of constant vorticity magnitude (streamwise and cross-stream components only $\Omega = (\Omega_x^2 + \Omega_y^2)^{1/2}$, magenta) and a surface of constant pressure (yellow). Note that a surface of constant streamwise vorticity will not depict a purely cross-stream segment of a rib vortex

https://doi.org/10.1017/jfm.2013.185 Published online by Cambridge University Press

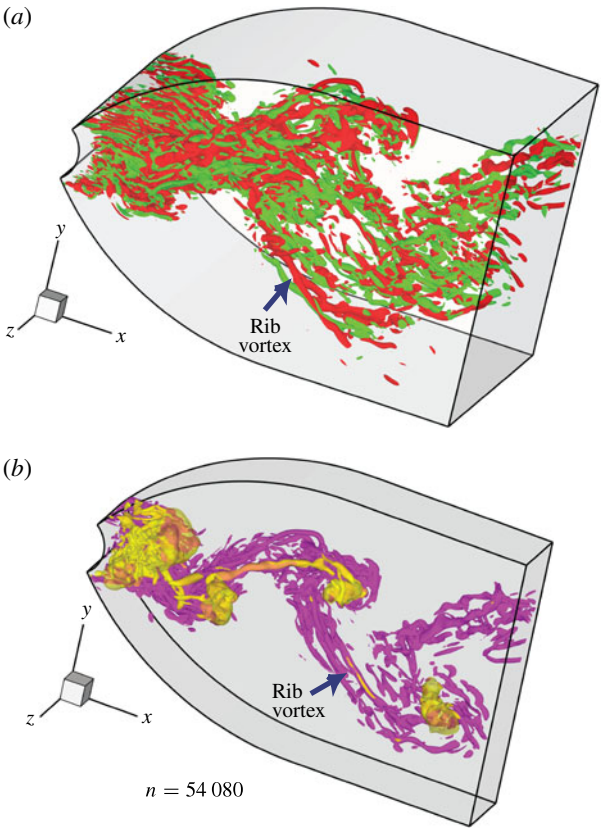


FIGURE 8. Perspective view of the wake region (up to $x/D = 7.0$): (*a*) surface of positive (red) and negative (green) streamwise vorticity, showing rib vortices (full span) and (*b*) surface of constant vorticity magnitude (magenta) and pressure (yellow), showing rib and shed vortices (25 % span).

and, similarly, a surface of constant cross-stream vorticity will not depict a purely streamwise segment of a rib vortex. The combination used here shows the structure of the rib vortices in the braid as well as their evolved versions in the core region. Figure 8(*b*) shows the ribs wrapping around the core. The surface of constant pressure shows the position of the cores. The elongated yellow segments within some of the ribs and enveloping others are indicative of a pressure minimum running the length of the ribs. Two-dimensional animations of vorticity show the ribs in a braid wrapping themselves around the two shed vortices at the ends of the braid. A top view shows that the majority of the ribs are aligned with the x-axis while some occur at significant angles to this direction.

Figure 9(*a*) is an end view (constant x plane) with instantaneous contours of streamwise vorticity at $x/D = 4.5$. The time instant is the same as that at which the data of figures 4 and 8 were obtained. It is evident from figure 4 that the location $x/D = 4.5$ is between two successive shed vortices and that the plane intersects the braid region. To a large extent this plane avoids the vortex cores. Cross-sections of the rib vortices are plentiful in this plane. Many of them occur as pairs, although a few seem to be isolated. Most of them are located below the centreline ($y/D = 0.0$)

https://doi.org/10.1017/jfm.2013.185 Published online by Cambridge University Press

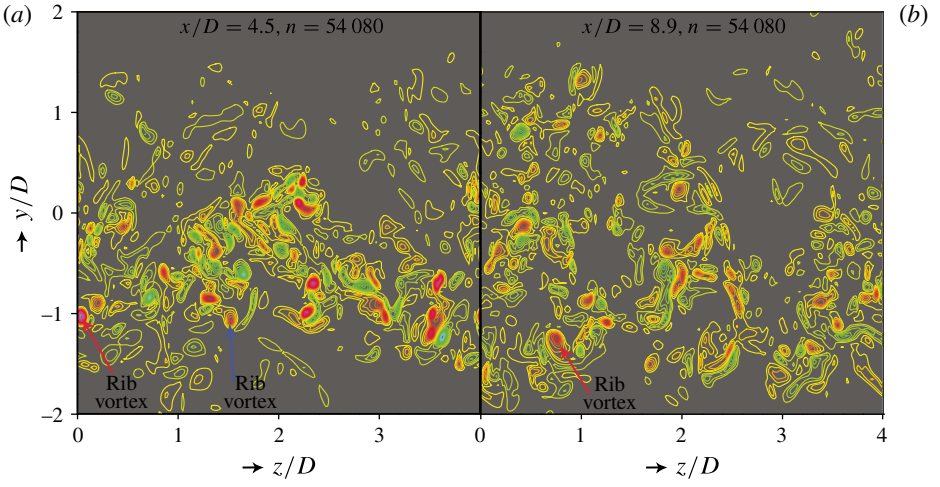


FIGURE 9. Instantaneous streamwise vorticity contours in an end plane: (*a*) $x/D = 4.5$ and (*b*) $x/D = 8.9$; red/magenta represent high/highest positive values, green/blue low/lowest negative values, yellow ≈ 0.0.

because the plane intersects the braid in a region where the braid is located below this line. The cross-sectional shapes vary from elongated ellipses to nearly circular ones. The near-circular cross-sections are $\sim 0.1D$ in 'diameter' whereas some of the elongated ones are as large as $0.35D$ in length. The actual cross-sections of the ribs are even smaller than in figure 9(*a*) because the plane cuts many ribs at a nominal angle of 45°. In comparison the shed vortices are $\sim 1.0D$ in diameter at this x location (figure 5) and thus much larger.

The peak vorticity values within the ribs are significantly higher than the corresponding phase-averaged peak values in the cores of the shed vortices. The rather strong rib indicated with a red arrow in figure 9(*a*) has a peak vorticity value that is ~9 times larger than the phase-averaged peak spanwise vorticity associated with the shed vortex at $x/D = 5.5$ in figure 5. Even the relatively weak one (blue arrow) has a peak value ~3.2 times that of the corresponding shed vortex. These ratios are misleading: peak instantaneous spanwise vorticity levels in the cores are much larger than the phase-averaged values.

Figure 9(*b*) is similar to figure 9(*a*) but the plane is located at $x/D = 8.9$. This plane is also located between successive shed vortices, cuts the braid and, to a large extent, avoids the shed vortices themselves. It shows some activity in the upper plane that is associated with the upper shed vortex. Figures 9(*a*) and 9(*b*) can be compared directly because, the minimum/maximum values of vorticity that are specified and, the increment in contour levels is the same. The ribs have weakened in figure 9(*b*). This is to be expected since the strain field in the braid in this region is weaker (the principal strain rates decrease by ~32 % between the saddle points just upstream of the positive vortex cores at $x/D = 5.5$ and 9.6, see figure 5). The peak vorticity values associated with the rib vortices continue to dominate the local phase-averaged peak vorticity in the shed vortices. The cross-sectional shapes and sizes in figure 9(*b*) are similar to those in figure 9(*a*). *In summary, the rib vortices in the region* $4.0 < x/D < 13.0$ *are considerably smaller in cross-sectional area than the shed vortices, and many of them*

https://doi.org/10.1017/jfm.2013.185 Published online by Cambridge University Press

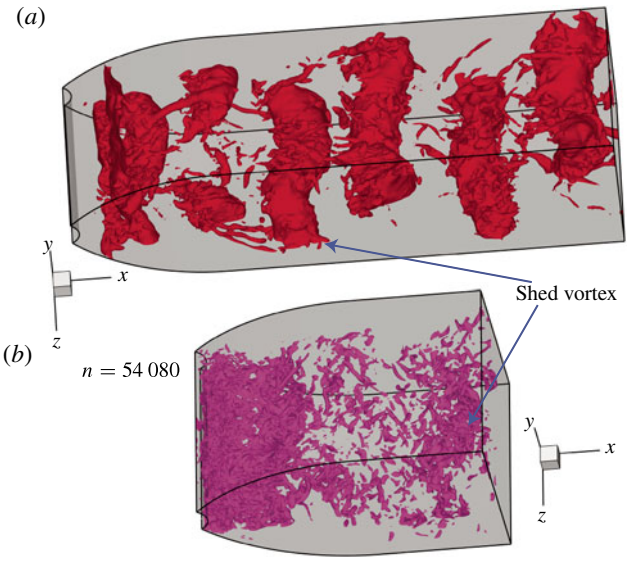


FIGURE 10. Perspective view of wake (full span): (*a*) surface of constant pressure, showing shed vortices and rib vortices (up to $x/D = 13.6$) and (*b*) surface of constant positive spanwise vorticity (up to $x/D = 7.0$).

possess peak vorticity values significantly higher than the phase-averaged spanwise vorticity of the corresponding shed vortices.

Figure 10(*a*) shows a constant pressure surface at the same time instant as in figure 8. The shed vortices are evident. Although there is some distortion of the structures it is rather limited except for one ruptured shed vortex (such ruptured vortices are infrequent). Figure 10(*a*) also shows signatures of the rib vortices (appearing as contorted tubes) and the shedding of a vortex at the plate trailing edge. Figure 10(*b*) shows a surface of constant *positive* spanwise vorticity at the same time instant. The vortex highlighted with an arrow is the one downstream of the ruptured vortex in figure 10(*a*) and is located below the wake centreline. Among the ones that are whole this shed vortex shows noticeable spanwise distortion. The core is populated with regions of spanwise vorticity that are elongated in the z direction, are roughly aligned with this direction and are confined to the central region of the shed vortex. They are intertwined and collectively form the core. There is no evidence of a single columnar structure at the centre. The vorticity magnitude used in figure 10(*b*) is three times the phase-averaged spanwise vorticity at $x/D = 7.6$, thus peak values in the core are much higher than the phase-averaged value.

To better illustrate the structure of the vortex core, figure 11(*a*) provides instantaneous spanwise vorticity contours in an end plane (y, z). This plane intersects the lower positive vortex at $x/D = 5.7$ at approximately its centre (figure 4 and the blue arrow in figure 10*b*). The fragmented nature of the core is evident. The level of fragmentation is expected since the vortices are formed by the roll-up of turbulent shear layers. Note that the region $1.0 < z/D < 3.0,\ y/D > 0.0$ corresponds to the braid and not the shed vortex.

The elongated positive vortices that comprise the core are evident ($y/D < 0.0$). Peak vorticity values are $\sim$5 times as large as the peak phase-averaged value at $x/D = 5.5$ (figure 5). Interspersed among them are regions of negative vorticity. They are weaker

https://doi.org/10.1017/jfm.2013.185 Published online by Cambridge University Press

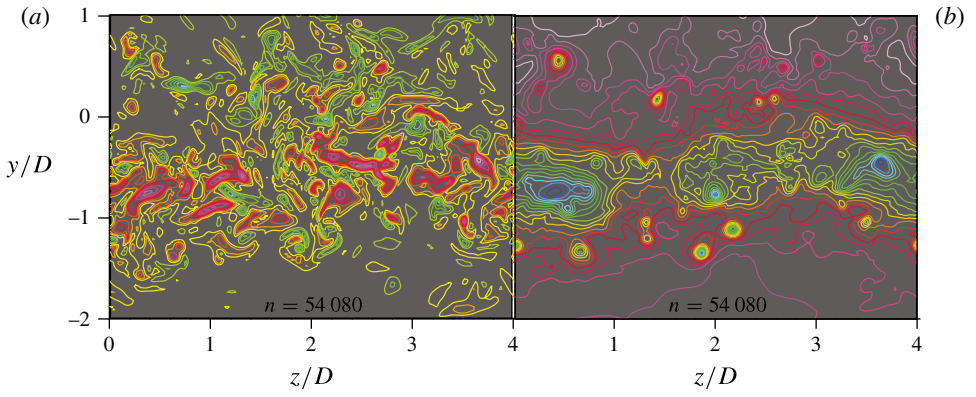


FIGURE 11. Contours of (*a*) spanwise vorticity (red/magenta represent high/highest positive values, green/blue low/lowest negative values, yellow ≈0.0) and (*b*) pressure in the end plane (y, z) at $x/D = 5.7$.

and in general do not have the characteristic shape of the positive vortices. Some of the negative vorticity is accumulated in the initial formation of the positive shed vortices when they in proximity to the turbulent shear layers from the opposing side. Figure 11(*b*) shows pressure contours in the same plane and time instant as in figure 11(*a*). The core as represented by the pressure does not show the level of fragmentation seen in figure 11(*a*). This is partly because it is not a derivative of a variable. Also it has been observed here that the pressure fields of closely spaced turbulent vortices merge into a single low-pressure region. The nearly circular pressure minima above and below the core in figure 11(*b*) are rib vortices that have wrapped themselves around the core as in figure 8.

In HH (1989) the three-dimensionality of the shed vortex is examined via two-point correlations of smoothed vorticity (vorticity integrated over time) as well as phase-averaged spanwise vorticity contours at multiple spanwise locations (figures 7 and 8 in HH (1989)). Two-point correlations decrease exponentially with increasing spanwise separation (Δz) and the peak spanwise vorticity decreases with increasing spanwise separation between the location at which phase is determined and the location at which vorticity is measured. Peak vorticity is halved for a spanwise separation of $2.0D$, thus indicating considerable vortex distortion. Various possible modes of distortion are discussed in HH (1989). Here, phase-averaged spanwise vorticity is computed at various z locations. In this exercise alone, vorticity is not averaged in the z direction, and phase is determined in a plane that is separated by a distance $2.0D$ in the z direction from the plane at which the phase averaging is performed. Contours of the computed vorticity at $z/D = 2.0$ (full lines) and $z/D = 4.0$ (dashed lines) are shown in figure 12 at $\phi = 0.0$. There is little difference in vortex shape and core location. The ratio of peak vorticity values (in these two planes) in the vortex whose centre is at about $x/D = 12.0$, is 0.99. The degree of distortion reported in HH (1989) is not present here. However, the two flows are different. More importantly, the largest value of x/D at which vortices are compared here is 12.0, whereas in HH (1989) the comparisons are further downstream ($x/D = 20.0$ and 40.0). Hence, a greater loss of coherency in vortex structure can be expected in the data of HH (1989).

https://doi.org/10.1017/jfm.2013.185 Published online by Cambridge University Press

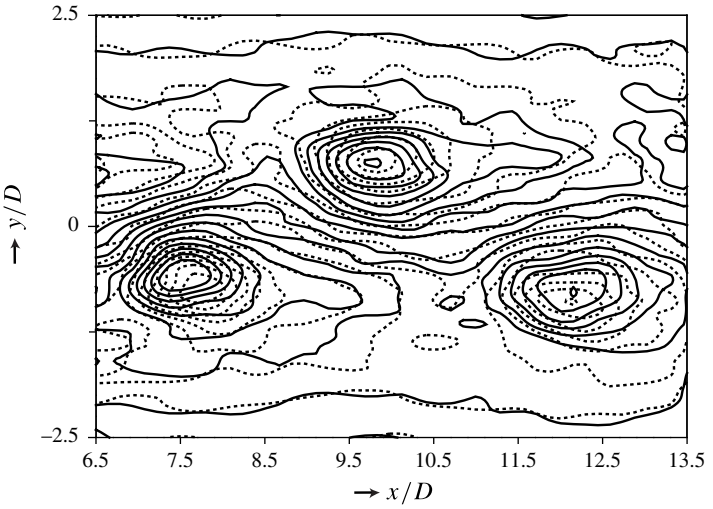


FIGURE 12. Phase-averaged vorticity contours (phase computed at $z/D = 2.0$) at $z/D = 2.0$ (full lines) and $z/D = 4.0$ (dashed lines).

3.5. *Production of vorticity in the near wake*

Much of the prior discussion and earlier research has dealt with rib vortices in the braid and the amplification of the streamwise and transverse vorticity associated with them by vortex stretching as a result of the phase-averaged strain rate. Here we probe the distribution of the fluctuating vorticity in the braid and core regions. As seen in figure 10(*a*) and (*b*) some ribs have a healthy spanwise component although the production of this component by the phase-averaged strain rate is zero. Figures 13(*a*)–13(*c*) show phase-averaged vorticity fluctuations $\langle\omega_i\omega_i\rangle$ where ω_i is the randomly fluctuating vorticity component in the ith direction ($i = 1, 2\ 3$ corresponding to the x, y and z directions, respectively). All of them have peaks near the cores and elevated values in the braids. The magnitude of the three components are comparable; the peak values near the core at $x/D = 5.5$ are approximately 6.2, 4.8 and 4.3, respectively. While rib vortex stretching is an important contributor to the production of ω_1 and ω_2, the questions that arise are: what other sources contribute to ω_1 and ω_2 and what is the source ω_3?

The transport equation for $\langle\omega_i\omega_j\rangle$, assuming incompressible flow, is given by

$$\frac{\partial\langle\omega_i\omega_j\rangle}{\partial t} + \langle u_k\rangle\frac{\partial\langle\omega_i\omega_j\rangle}{\partial x_k} = R_1 + R_2 + R_3 + R_4 + R_5 + R_6 + R_7 \qquad (3.4a)$$

$$R_1 = -\left(\langle\omega_i u_k'\rangle\frac{\partial\Omega_j}{\partial x_k} + \langle\omega_j u_k'\rangle\frac{\partial\Omega_i}{\partial x_k}\right) \quad R_2 = -\frac{\partial\langle\omega_i\omega_j u_k'\rangle}{\partial x_k} \qquad (3.4b)$$

$$R_3 = \langle\omega_j\omega_k s_{ik}\rangle + \langle\omega_i\omega_k s_{jk}\rangle \quad R_4 = \langle\omega_j\omega_k\rangle S_{ik} + \langle\omega_i\omega_k\rangle S_{jk} \qquad (3.4c)$$

$$R_5 = \Omega_k(\langle\omega_j s_{ik}\rangle + \langle\omega_i s_{jk}\rangle) \quad R_6 = \nu\frac{\partial^2\langle\omega_i\omega_j\rangle}{\partial x_k\partial x_k} \quad R_7 = -2\nu\left\langle\frac{\partial\omega_i}{\partial x_k}\frac{\partial\omega_j}{\partial x_k}\right\rangle. \qquad (3.4d)$$

In (3.4), Ω_i is the phase-averaged vorticity component in the ith direction and s_{ij} and S_{ij} are the fluctuating (random) and phase-averaged strain-rate tensors, respectively.

https://doi.org/10.1017/jfm.2013.185 Published online by Cambridge University Press

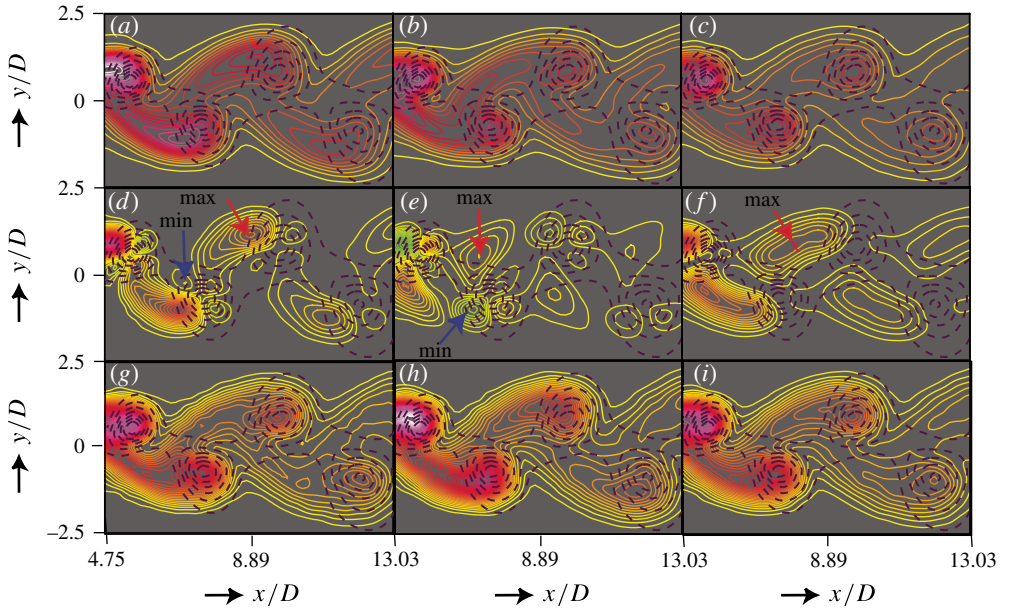


FIGURE 13. Phase-averaged distributions of (*a*) $\langle\omega_1\omega_1\rangle$, (*b*) $\langle\omega_2\omega_2\rangle$ and (*c*) $\langle\omega_3\omega_3\rangle$; of the production term R_4 in the transport equation for (*d*) $\langle\omega_1\omega_1\rangle$, (*e*) $\langle\omega_2\omega_2\rangle$ and (*f*) $\langle\omega_1\omega_1\rangle + \langle\omega_2\omega_2\rangle$; and of the production term R_3 in the transport equation for (*g*) $\langle\omega_1\omega_1\rangle$, (*h*) $\langle\omega_2\omega_2\rangle$ and (*i*) $\langle\omega_3\omega_3\rangle$; red/magenta represent high/highest positive values, green/blue low/lowest negative values, yellow ≈ 0.

The fluctuating (random) and phase-averaged velocity components are denoted by u_k' and $\langle u_k\rangle$, the coordinates in the x, y and z directions by x_k and ν is the kinematic viscosity. Equation (3.4) is an extension of the transport equation obtained when the mean flow is steady. Assuming that the periodic fluctuating component is absent and $j = i$ and replacing the phase averages with time averages, we obtain the corresponding equation of Tennekes & Lumley (1972). The terms on the right-hand side of (3.4) represent the exchange of vorticity between $\langle\omega_i\omega_j\rangle$ and $\langle\Omega_i\Omega_j\rangle$ (R_1), turbulent transport (R_2), production by turbulent stretching (R_3), production by phase-averaged strain rate (R_4), a mixed production term (R_5), viscous transport (R_6) and dissipation (R_7). The terms R_2, R_6 and R_7 are not discussed here since the interest is in the production of turbulent vorticity. Further, because the terms R_1 and R_5 are significantly smaller than R_3 and R_4 (peak values of R_1 and R_5 are less than 5 % of the corresponding peaks in R_3 and R_4) the former two are not discussed. The emphasis is on R_3 (turbulent stretching) and R_4 (a significant contributor to rib vortex stretching) and their relative importance in the vorticity dynamics of the near wake of the flat plate.

Figure 13(*d*) and (*e*) show the distribution of the production term R_4 for the quantities $\langle\omega_1\omega_1\rangle$ and $\langle\omega_2\omega_2\rangle$, respectively. Figure 13(*d*) shows a positive peak upstream of each core (red arrow). This is consistent with the fact that rib vortices are largely aligned with the x direction in this location and thus contain predominantly streamwise vorticity; rib vortex stretching would thus produce additional fluctuating streamwise vorticity, $\langle\omega_1\omega_1\rangle$. Likewise in figure 13(*e*), we see a positive peak (red arrow) below negative vortex cores and above positive vortices. This is consistent with the fact that rib vortices are mostly oriented with the y-axis in these regions.

https://doi.org/10.1017/jfm.2013.185 Published online by Cambridge University Press

Thus stretching of rib vortices results in the production of $\langle\omega_2\omega_2\rangle$. Both of these figures also show regions of consumption (blue arrows). Peak consumption in one component coincides with peak production in the other indicating a transfer of energy from one component to the other and is consistent with rib alignment with the braid. Figure 13(*f*) shows the sum of the two production rates. It is positive everywhere and as expected resembles the distribution of the production rate of TKE in figure 7(*c*).

Figure 13(*g*)–(*i*) show the distribution of the production term R_3 associated with turbulent stretching of turbulent vorticity, for the three components $\langle\omega_i\omega_i\rangle$, $i = 1, 3$, respectively. First, they closely correspond to the distributions of vorticity fluctuation in figure 13(*a*)–(*c*). The distributions obtained for the three components are very similar. They show peak values near the cores and significant magnitudes in the braids. Second, they are positive everywhere. The ratios of the three components of R_3 to the combined value of R_4 in figure 13(*f*) at the position marked with an '*x*' (local maximum due to phase-averaged strain rate) are 1.45, 1.70 and 1.55, respectively. The ratios of the peak value for the three components near the negative core at $x/D = 7.6$ to the value of R_4 at the location marked with an '*x*' are 3.60, 4.45 and 3.40, respectively. The ratio of the integrated value of R_3 (three components combined) to the value of R_4 (two components combined) in the region $5.5 < x/D < 9.8$ (distance between subsequent negative vortices at $\phi = 0.0$), $-2.5 < y/D < 2.5$ is ~9.47. Thus, the stretching of rib vortices via the phase-averaged strain rate produces significantly less turbulent vorticity than that produced by turbulent stretching both in the braids and in the cores. In particular, figure 13(*i*) shows the importance of turbulent stretching in sustaining fluctuations in the spanwise component of vorticity.

3.6. *Analysis of the time-varying data at specified streamwise locations*

KM (1988) present experimentally obtained wake data for a normal plate (face normal to the flow direction) at a distance $8h$ from the plate, h being the dimension of the plate in the cross-stream direction. The distribution of the TKE and turbulent shear stress at different phases and within specified frequency ranges is computed. Phase averaging is accomplished using a reference signal that is a band-pass filtered time history of the cross-stream velocity, v, at the wake centreline and at a streamwise distance of 8 h from the plate. The mean vortex-shedding frequency is used as the central frequency of the filter. The zero crossings of the reference signal are then determined and the time periods between them are either dilated or compressed as necessary to match half the average shedding period. Once this is accomplished, the phase at a given point in time is easily established, and given a phase, the corresponding time instants can be determined. Phase-averaged data thus obtained (distributions of velocities, intensities, etc.) are at a given x location ($x = 8h$). Hence, unlike in the present study, the distributions of KM (1988) do not provide the streamwise evolution of turbulent stresses. Now we compare the phase-averaged distributions of normal intensities and shear stress (random component) obtained using a phase-averaging method very similar to that of Matsumura & Antonia (1993) and KM (1988) with those computed using the phase-averaging method developed here (appendix B).

We use the time variation of the cross-stream velocity v at $x/D = 5.5$ and $y/D = 0.0$ to determine phase with the present computed data, via the method of KM (1988). The computed waveform is first z-averaged and then band-pass filtered as described earlier. The zero crossings of the filtered waveform are then determined. Figure 14(*a*) shows the z-averaged waveform, the filtered waveform and the zero crossings over 10 000 time steps (~5.7 shedding periods) at the location of the vortex core at $x/D = 5.5$

https://doi.org/10.1017/jfm.2013.185 Published online by Cambridge University Press

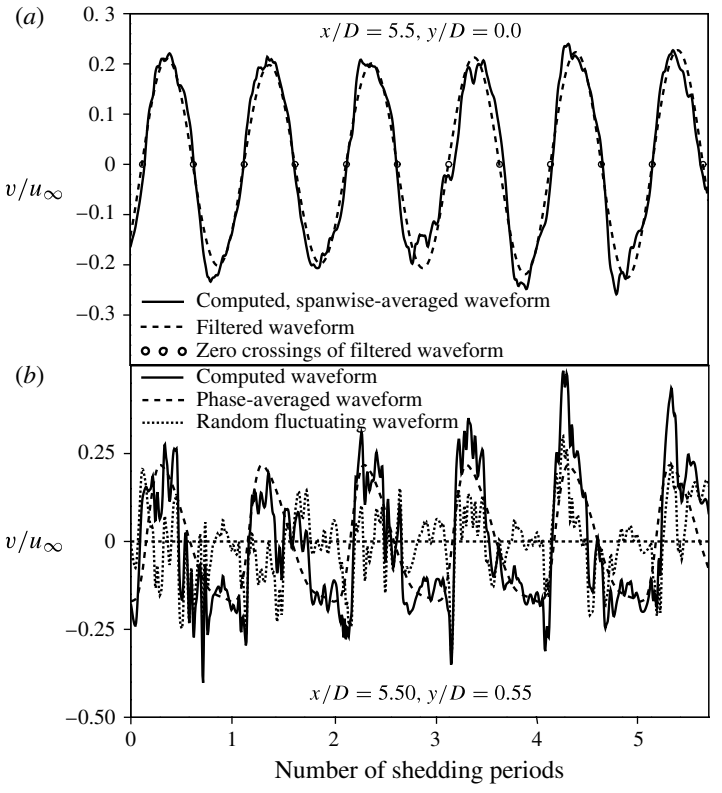


FIGURE 14. (*a*) The spanwise-averaged (computed) and filtered (reference) waveforms and the zero crossings of the filtered waveform; (*b*) the computed, phase-averaged and randomly fluctuating cross-stream velocity waveform (near the vortex core).

in figure 5. Phase at any given time or the times at which a certain phase occurs are determined as described earlier. Figure 14(*b*) shows the computed value of v, the phase-averaged waveform and the turbulent waveform (the difference of the former two waveforms, see (3.1) and (3.2)). The phase-averaged waveform needs to be compressed or dilated as necessary based on the locations of the zero crossings of the reference signal to obtain the time variation of the quasi-periodic waveform. The phase-averaged data (normal intensities, etc.) at any y location can then be obtained. Note that the implied transformations in time, from the dilations/compressions, are not slope continuous at the zero crossings.

Figure 15 shows the normal intensities and shear stress (random component) obtained using the phase-averaging method of Matsumura & Antonia (1993) and KM (1988). This figure is the counterpart to figure 6 (where the results are obtained using the phase-averaging method developed in the present study). The data plotted in figure 15 are obtained from the computed velocity signals at $x/D = 5.5$; streamwise feature evolution is absent in figure 15. However, the results of figure 15 can be compared with those of figure 6 in the vicinity of $x/D = 5.5$. Visually, the two figures are very similar. Features such as vortex cores, braids, minima/maxima are in agreement. A quantitative comparison also shows good agreement between the two sets of results. For example the ratio of the turbulent stresses at the vortex

https://doi.org/10.1017/jfm.2013.185 Published online by Cambridge University Press

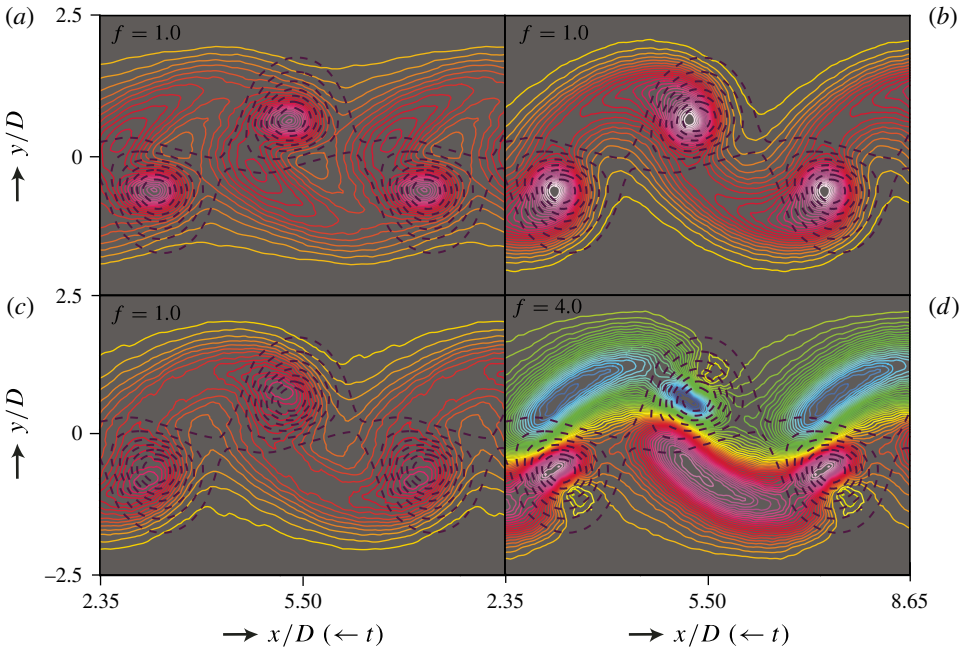


FIGURE 15. Contours of (*a*) $\langle u'u'\rangle$; (*b*) $\langle v'v'\rangle$; (*c*) $\langle w'w'\rangle$ and (*d*) $\langle u'v'\rangle$ and $\langle p\rangle$; red/magenta represent high/highest positive values, green/blue low/lowest negative values, yellow ≈0.0.

cores ($x/D = 5.5$, random component) are 1.08, 1.02, 1.01 and 1.07 ($\langle u'u'\rangle$,$\langle v'v'\rangle$, $\langle w'w'\rangle$ and $\langle u'v'\rangle$, respectively). This ratio is defined as the data obtained using the phase-averaging method developed here (appendix B) divided by that obtained with the method of KM (1988) and Matsumura & Antonia (1993). The periodic component of stresses obtained using the two phase-averaging methods are also in good agreement. Clearly the two methods yield comparable results when restricted to a given x location.

An important finding of KM (1988) is that the real part of the cross-spectrum of the u' and v' signals (turbulent shear stress) shows a dominant peak at about half the shedding frequency ω_{st} whereas the power spectra of u', v' and w' show peaks located between ω_{st} and $2\omega_{st}$ (figures 6 and 7 in KM (1988)). A frequency-based analysis of the data, that is, an identification of the contributions of different frequency ranges to the overall distribution of a given quantity, is provided in KM (1988). The dominant frequencies in different regions of the wake such as the braid or the vortex core can be obtained using this analysis. Frequency-based distributions are obtained via band-pass filters with the central frequency specified to be an integral or fraction of ω_{st}. The TKE and shear stress distributions (random component) with the filter centred at $\omega/\omega_{st} = 0.5$, 1.0, 2.0 and 3.0 are provided in KM (1988). The shear stress distributions thus obtained also show that the dominant contributor to shear stress is the frequency range centred at $\omega/\omega_{st} = 0.5$. A possible explanation for this phenomenon is provided in KM (1988). It is theorized that the rib placements on alternate shed vortices, on one side of the wake centreline, are similar, thus causing deformations in these alternate vortices to be similar; this, in turn, results in significant contributions to the subharmonic.

https://doi.org/10.1017/jfm.2013.185 Published online by Cambridge University Press

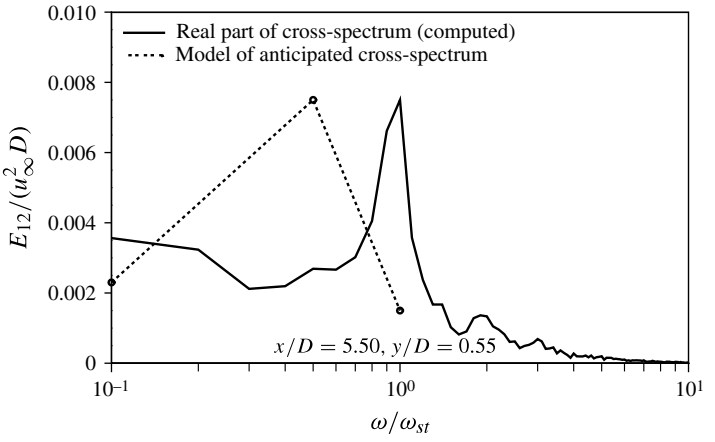


FIGURE 16. Real part of cross-spectrum for u' and v'.

This finding of KM (1988) raises some interesting questions. Is the dominant subharmonic exhibited by the turbulent shear stress (and only the turbulent shear stress) a universal feature of turbulent wakes? If not, what are the defining characteristics of wakes that fall in this category of possessing a dominant subharmonic (say **KM1**) and those that do not (**KM2**)? The cross-spectrum for the u' and v' signals was computed using the current data to determine if the dominant subharmonic is present here as well. Figure 16 shows the computed cross-spectrum and the anticipated one in the case of a dominant subharmonic. The latter is modelled after the cross-spectrum of KM (1988) with the peak value set equal to the computed peak obtained at $\omega/\omega_{st} = 1.0$; the values on either side ($\omega/\omega_{st} = 0.1$ and 1.0) were estimated from the trends in KM (1988). Clearly, the computed peak occurs at shedding frequency and not at about half the shedding frequency. Thus, the present data show that the dominant subharmonic peak of KM (1988) is not a universal feature of the turbulent near wake.

4. Concluding remarks

The near wake of a thick flat plate with a CTE, with pronounced shedding of wake vortices, is investigated via DNS. The emphasis in the present study is on the vortical structures of the near wake, phase-averaged distributions of the random component of normal intensities, shear stress and vorticity fluctuations and the distribution of the production terms in the corresponding budgets.

The high resolution obtained in a DNS (time-varying, three-dimensional data) provides us with an unprecedented ability to understand the complicated physics of the wake being investigated. A first effort at visualizing some of the important features of the near wake, such as the strength and structure of rib vortices in relation to the shed vortices, their evolution in time, the internal structure of shed vortices, etc., are provided here. Some of the findings are as expected (rib vortices in the braids) while others such as the presence of intense elongated spanwise vortices and the absence of a single columnar vortex in the cores provide new understanding of the cores and braids and the interaction between them. The dataset that has been generated holds a wealth of information that is yet to be mined with both snapshots in time as well as animations and statistical analysis. In particular, the base region where the

https://doi.org/10.1017/jfm.2013.185 Published online by Cambridge University Press

separated turbulent boundary layers and the recirculation region interact promises to yield insights that are first-of-a-kind and much needed in both aerofoil design and turbulence modelling efforts. Notably, the present DNS dataset permits an analysis of the velocity, pressure and temperature fields.

Distributions of the phase-averaged turbulent intensity and shear stress (random component) in the near wake are explored and compared with those of CC (1983). While some of the features in these distributions are the same as in CC (1983) (for example, the maximum in two components of the intensity near the vortex cores, peak shear stress values in the braids etc.), some of them are not (such as the maximum in $\langle u'u' \rangle$ in the braids). Some of these differences may be directly attributed to the high resolution obtained in the DNS while others are probably a result of the differences in the basic flow. Attributing the differences in flow features to one of these reasons requires a DNS of the cylinder at $Re_D = 140\,000$ (or an experiment with equivalent resolution). However, the present investigation meets the objective of establishing the flow physics encountered in the near wake of the flat plate. Wherever possible a physical explanation of the origin of the important features of the distributions, as well as one based on the distribution of the production term in the corresponding budget, is provided.

Phase-averaged values are obtained here using a conceptually different procedure than employed in CC (1983). The appearance of the shed vortex at a particular x location is ascribed a certain phase; different phase values are obtained as the vortex moves to different locations downstream. The relationship between vortex location and phase is established. This approach to phase averaging is easy to implement and yields crisp, well-defined braid and vortex structure.

Earlier research has primarily dealt with rib vortices as they occur in the braid and the amplification of the streamwise and transverse vorticity associated with them by vortex stretching as a result of the associated strain rate. Here it is found that on average the stretching of rib vortices via the phase-averaged strain rate produces significantly less turbulent vorticity than that produced by turbulent stretching both in the braids and in the cores. In particular, the data show the importance of turbulent stretching in sustaining fluctuations in the spanwise component of vorticity.

An analysis of the time-varying velocity signals at $x/D = 5.5$ is provided. Phase-averaged data at this location are obtained as in KM (1988) and Matsumura & Antonia (1993). The reasons for this analysis are twofold: first, to compare the periodic and random turbulent intensity and shear stress distributions obtained with the phase-averaging method presented here and those obtained with methods of KM (1988) and Matsumura & Antonia (1993) and, second, to determine whether the cross-spectrum of the shear stress contains a peak at subharmonic frequency as in KM (1988). The intensity and shear stress distributions obtained using both methods are quite similar. However, the cross-spectrum for the computed shear stress peaked at ω_{st} and not at $0.5\omega_{st}$. Thus, the dominant subharmonic peak of KM (1988) is not a universal feature of the turbulent near wake.

Acknowledgements

The contents of this paper were originally presented in AIAA Meeting Papers 2008-0544 (AIAA 46th ASM, January 2008, Reno, Nevada), 2011-3575 (AIAA 41st FDM, June 2011, Honolulu, Hawaii) and 2012-0067 (AIAA 50th ASM, January 2012, Nashville, Tennessee).

https://doi.org/10.1017/jfm.2013.185 Published online by Cambridge University Press

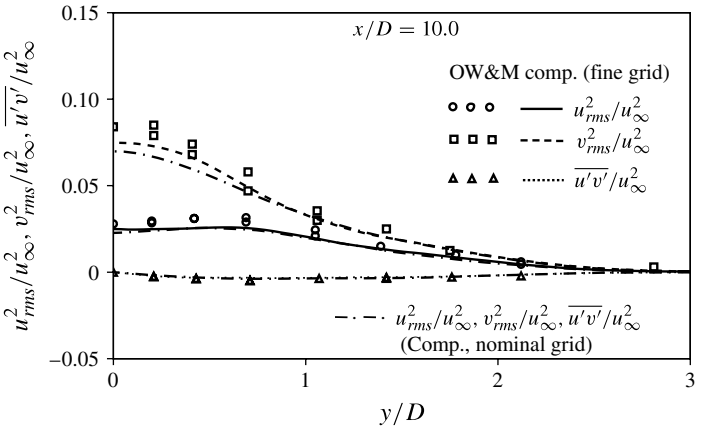


FIGURE 17. Intensity and shear stress profiles for the cylinder at $Re_D = 3900$ ($x/D = 10.0$).

Appendix A. Adequacy of computational domain and grid resolution

The resolution achieved in the x, y and z directions at $x/D = 10.0$, $y/D = 0.0$, is approximately $\Delta x/\eta = 4.0$, $\Delta y/\eta = 4.0$ and $\Delta z/\eta = 2.1$, where η is the computed Kolmogorov length scale at this location. Closer to the base at $x/D = 5.5$ the grid spacing based on this length scale are 12.5 % larger. A grid resolution study where the grid is refined and convergence of the solution with refinement is demonstrated would be ideal. However, because of the large computational costs involved, here we compare experimental and computed data (obtained with similar resolution in an earlier study by Rai (2008)) for a cylinder wake to demonstrate that the resolution used for the flat plate wake is adequate. The computational method is the same in both cases. The cylinder wake computation corresponds to the experimental investigation of Ong, Wallace & Moin (1995) at $Re_D = 3900$. The separating boundary layers are laminar. The computation was performed on a nominal grid with 1 368 576 grid points and a fine grid with 2 941 920 grid points and is discussed at length in Rai (2008). The resolution obtained at $x/D = 10.0$ with the nominal grid was $\Delta x/\eta = 5.6$, $\Delta y/\eta = 5.7$ and $\Delta z/\eta = 6.5$ and that with the fine grid was $\Delta x/\eta = 4.1$, $\Delta y/\eta = 3.8$ and $\Delta z/\eta = 5.2$. The resolution in the x and y directions in the flat plate simulation is nearly the same as that obtained with the fine grid. In the z direction it is much finer in the plate computation.

Figure 17 compares computed and experimental intensities and shear stress (total values) at $x/D = 10.0$. The data obtained with the fine grid compare well with the experimental data. The nominal grid yields a v^2_{rms} profile that is slightly lower. Figure 18 compares one-dimensional spectra (E_{11}) obtained in the experiment and in the two computations at $x/D = 10.0$, $y/D = 0.0$. The computed spectra have been truncated so that only the energy in the resolvable scales (cutoff frequency determined using Taylor's hypothesis) appears in the figure. The computed and experimental data agree well over a reduction in magnitude of ∼500; there is some dissipation at the smaller scales ($\omega/\omega_{st} > 10.0$).

The external boundary of the plate zone is placed $50.0D$ from the surface of the plate and the leading edge, and the exit boundary is placed $104.0D$ from the trailing edge. Past experience with plate and cylinder flows has proved this placement to be adequate. In comparison, the cylinder LES of Kravchenko & Moin (2000) uses

https://doi.org/10.1017/jfm.2013.185 Published online by Cambridge University Press

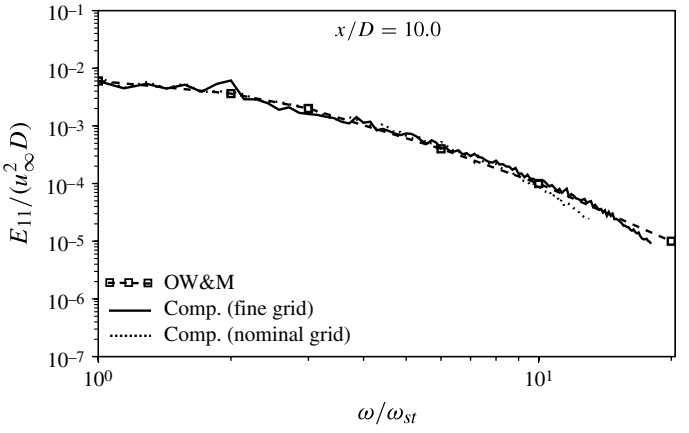


FIGURE 18. Spectrum of the streamwise velocity component for the cylinder at $Re_D = 3900$ ($x/D = 10.0$).

a cylindrical outer boundary between $15.0D$ and $30.0D$ (two different computations, $Re_D = 3900$). The size of the computational domain in the z direction (homogeneity with periodic boundary conditions) is πD; this choice is based on the investigation of Chyu & Rockwell (1996) where the wavelengths of the larger structures in the z direction were found to be of the order of $1.0D$. In a more recent computation Dong *et al.* (2006) place the computational boundaries at $-20.0D$ and $50.0D$ in the x direction and $-20.0D$ and $20.0D$ in the y direction for a cylinder DNS ($Re_D = 10\,000$). The size of the domain in the z direction at this Reynolds number is again πD. The boundary placement used in the present investigation in the (x, y) plane exceeds what is considered adequate in the literature, and it is comparable in the z direction ($4.0D$).

The grid resolution in the plate grid in the x, y and z directions is $\sim$18.0, 0.84 and 6.5 wall units, respectively, based on the wall shear velocity near the end of the plate. A DNS of fully developed turbulent channel flow ($Re = 180$ based on channel half-width) using upwind-biased differences as in the present computation, but with a lower order of accuracy is provided in Rai & Moin (1991). The resolution used there in the x and z directions are $\sim$11.8 and 5.9 (a direct comparison in the wall-normal direction cannot be made because of the staggered-grid approach that is used in the channel flow DNS, however it is comparable with that used here). The total number of grid points used in the finite difference computation was 3 723 264. The computed data were compared with data obtained using a spectral method with 3 962 880 grid points (Kim, Moin & Moser 1987). Intensity profiles across the channel, near-wall behaviour of the intensities (intensities normalized by local mean velocity), vorticity fluctuations normalized by mean shear, and skewness factors, obtained in the two simulations, are compared and found to be in excellent agreement. These results show that high-order accurate upwind-biased finite-difference methods yield results that are comparable with those obtained with spectral methods. The upwind-biased differences used for the channel flow were fifth-order accurate (fifth-order dissipation terms). Here we use sixth- and seventh-order upwind-biased differences both with seventh-order dissipation terms. The viscous terms are computed with fourth-order central differences and the method is second-order accurate in time.

https://doi.org/10.1017/jfm.2013.185 Published online by Cambridge University Press

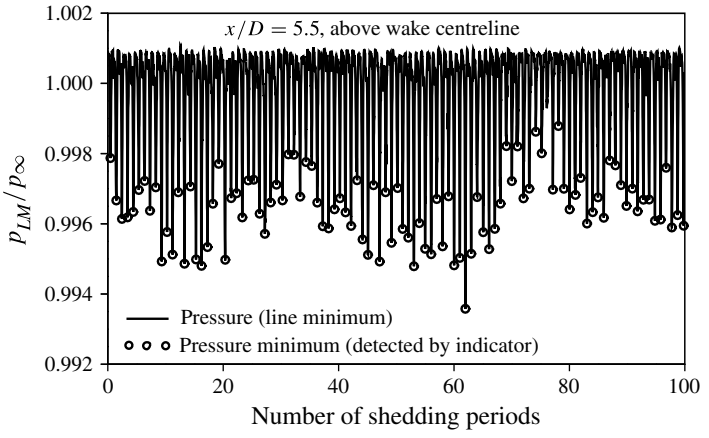


FIGURE 19. Line minimum of z-averaged pressure at $x/D = 5.5$ plotted as a function of time (upper wake).

Appendix B. Phase- and time-averaging methods

B.1. *Phase-averaging method*

In CC (1983) phase is determined by monitoring the time-varying pressure on the cylinder surface at 65° from the leading edge. Here phase is defined using an event-tracking approach that is conceptually different. Each phase is marked by a distinct easily recognizable event. The arrival of the vortex core at a given x location corresponds to a particular phase. The passage of a vortex core past any location results in a local minimum in the pressure signal. Hence, the time-variation of the z-averaged pressure at this x location is analysed. For the region above the centreline, the minimum z-averaged pressure that occurs from a specified distance above $y = 0.0$, all the way to the outer boundary of the wake region is computed (line minimum). The time variation of this line minimum is plotted in figure 19. The arrival of the vortex cores at $x/D = 5.5$ (upper half of the wake) is evident. A simple procedure that locates the pressure minima is used to determine vortex-core arrival times (shown with circles). This method is very effective in defining phase. Time occurrences of maximum/minimum amplitude in the spanwise-averaged cross-stream velocity can also be used instead to define phase (see figure 14*a*).

The phase average of a flow variable is obtained by averaging this variable at the points in time shown by the circles. The value of the phase ϕ is defined as being 0.0 when a vortex core above the centreline arrives at $x/D = 5.5$ (this choice is arbitrary). It is also the phase at which the previously shed vortex in the upper half of the wake arrives at $x/D = 9.8$. The phase varies between 0.0 and 1.0 as the vortex at $x/D = 5.5$ moves to the location $x/D = 9.8$. Here we define 29 equally spaced locations along the centreline between these two positions resulting in 31 locations at which pressure is monitored. The arrival of the vortex at these locations (increasing x) marks a different value of ϕ (increasing ϕ). In summary the phase-averaging method used here comprises the following three important aspects. (i) A method of determining phase (vortex arrival at given x, say x_v). (ii) A way of establishing different phases (varying x_v). (iii) Defining the relationship between phase and the easily identifiable quantity x_v. The phase averages of various quantities thus obtained show clear braid and vortex structure. In addition the method itself is simple to implement. Computing phase

https://doi.org/10.1017/jfm.2013.185 Published online by Cambridge University Press

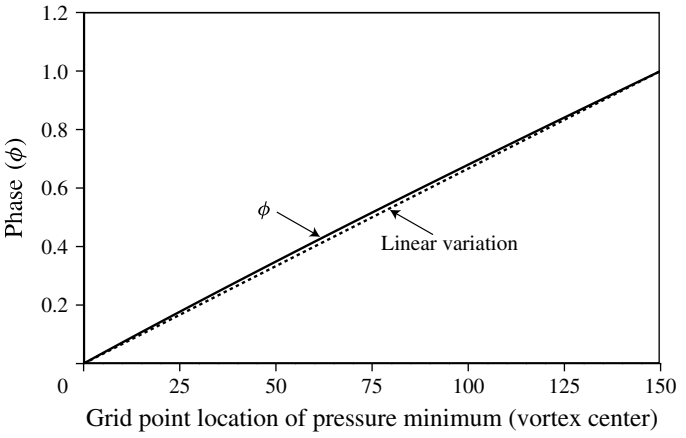


FIGURE 20. Phase ϕ plotted as a function of x along the wake centreline (from $x/D = 5.5$ to $x/D = 9.8$).

averages is different than the coherent structure extraction technique of HH (1989). The former concept implies capturing snapshots at similar points in time and averaging them whereas the latter involves tracking coherent structures in space and time.

B.2. *Time-averaging method*

The time average of a variable is obtained by integrating the distribution of the variable over all phases. The relationship between the phase ϕ and the corresponding x location of the vortex core is not linear. Although the spacing in x between subsequent locations of the vortex core at which phase-averages are computed is equal, the arrival of a vortex at consecutive locations does not mark equal increments in ϕ because the rate at which the vortex travels is not a constant, it increases with x. Here the time-averaged centreline velocity $u(x)$ is used to define the relationship between the vortex position and ϕ (starting at $x/D = 5.5$ and $\phi = 0.0$). The relationship is defined by the integral

$$K\varphi = \int_{5.5D}^{x} \frac{\mathrm{d}x}{u(x)}. \tag{B 1}$$

In (B 1), K is a constant that can be determined since at $x = 9.8D$ (integral upper limit), $\phi = 1.0$. The lower the velocity $u(x)$ the longer it takes to move between consecutive grid point locations even though they are equally spaced (thus resulting in a $\Delta\phi$ that is larger than the average value). Figure 20 shows the relationship between vortex location and phase obtained using (B 1); it is nearly linear. At $x/D = 5.5$ ϕ varies more rapidly than x because $u(x)$ is lower. The trend is reversed at the right extreme. Time averages are computed from phase averages using the dependence of ϕ on x seen in figure 20. Although the difference between the correct approach and a linear approximation is small, the point is discussed because the phase-averaging method used is conceptually different from that of CC (1983) and KM (1988).

REFERENCES

CANTWELL, B. & COLES, D. 1983 An experimental study of entrainment and transport in the turbulent near wake of a circular cylinder. *J. Fluid Mech.* **136**, 321.

https://doi.org/10.1017/jfm.2013.185 Published online by Cambridge University Press

CHEVRAY, R. & KOVASZNAY, L. S. G. 1969 Turbulence measurements in the wake of a thin flat plate. *AIAA J.* **7**, 1641.

CHYU, C. K. & ROCKWELL, D. 1996 Near wake structure of an oscillating cylinder: effect of controlled shear-layer vortices. *J. Fluid Mech.* **322**, 21.

DONG, S., KARNIADAKIS, G. E., EKMEKCI, A. & ROCKWELL, D. 2006 A combined direct numerical simulation–particle image velocimetry study of the turbulent near wake. *J. Fluid Mech.* **569**, 185.

HAJI-HAIDARI, A. & SMITH, C. R. 1984 A comparative study of the development of the turbulent near wake behind a thick flat plate with both a circular and tapered trailing edge geometry. Report No. FM-6, Department of Mechanical Engineering and Mechanics, Lehigh University.

HAYAKAWA, M. & HUSSAIN, F. 1989 Three-dimensionality of organized structures in a plane turbulent wake. *J. Fluid Mech.* **206**, 375.

KARLSON, R. I. & JOHANSSON, T. G. 1988 LDV Measurements of higher-order moments of velocity fluctuations in a turbulent boundary layer. Laser Anemometry in Fluid Mechanics, Ladoan-Instituto Superior Tecnico, Portugal.

KIM, J., MOIN, P. & MOSER, R. 1987 Turbulence statistics in fully developed channel flow at low Reynolds number. *J. Fluid Mech.* **177**, 133.

KIYA, M. & MATSUMURA, M. 1988 Incoherent turbulent structure in the near wake of a normal plate. *J. Fluid Mech.* **190**, 343.

KRAVCHENKO, A. G. & MOIN, P. 2000 Numerical studies of flow over a circular cyinder at $Re_D = 3900$. *Phys. Fluids* **12** (2), 403.

MANSOUR, N. N., KIM, J. & MOIN, P. 1988 Reynolds-stress and dissipation-rate budgets in a turbulent channel flow. *J. Fluid Mech.* **194**, 15.

MATSUMURA, M. & ANTONIA, R. A. 1993 Momentum and heat transport in the turbulent intermediate wake of a circular cylinder. *J. Fluid Mech.* **250**, 651.

ONG, L., WALLACE, J. & MOIN, P. 1995 The velocity and vorticity fields of the turbulent near wake of a circular cylinder. NASA TM -110513.

RAI, M. M. 2008 Towards direct numerical simulations of turbulent wakes. *Paper* 2008-0544, 46th AIAA Aerospace Sciences Meeting, Reno, Nevada.

RAI, M. M. 2010*a* Direct numerical simulations of the transitional/turbulent wake of a flat plate. *AIAA J. Propulsion Power* **26** (3), 575.

RAI, M. M. 2010*b* Direct numerical simulation of transitional and turbulent flow on a turbine airfoil. *AIAA J. Propulsion Power* **26** (3), 587.

RAI, M. M. 2011 Flow physics and self-similarity in the turbulent near wake of a flat plate. *Paper* 2011-3575, 41st AIAA Fluid Dynamics Conference, Honolulu, Hawaii.

RAI, M. M. 2012 Phase-averaged Reynolds-stress budget in the turbulent near wake of a flat plate. *Paper* 2012-0067, 50th AIAA Aerospace Sciences Meeting, Nashville, Tennessee.

RAI, M. M. & MOIN, P. 1991 Direct simulations of turbulent flow using finite-difference schemes. *J. Comput. Phys.* **96** (1), 15.

REYNOLDS, W. C. & HUSSAIN, A. K. M. F. 1972 The mechanics of an organized wave in turbulent shear flow. Part 3. Theoretical models and comparisons with experiments. *J. Fluid Mech.* **54**, 263.

TENNEKES, H. & LUMLEY, J. L. 1972 *A First Course in Turbulence*. MIT Press.

https://doi.org/10.1017/jfm.2013.185 Published online by Cambridge University Press